



# Uncertainty quantification of inflow on passive scalar dispersion in an urban environment

Bharathi Boppana<sup>1</sup> · Vinh-Tan Nguyen<sup>1</sup> · Daniel J. Wise<sup>1</sup> · Jason Yu Chuan Leong<sup>1</sup>

Received: 27 December 2022 / Accepted: 23 April 2023  
© The Author(s), under exclusive licence to Springer Nature B.V. 2023

## Abstract

Risk assessment, city planning, and emergency response are a few examples of potential applications of numerical simulations of scalar dispersion in urban environments. The complex flow fields and scalar dispersion are determined by the building layout and prevailing meteorological conditions that are highly uncertain. While the fidelity of a numerical model is important in providing an accurate prediction of flow and scalar fields, propagating the uncertain input through numerical models is imperative in those applications. However, it is uncommon to quantify input uncertainties due to expensive computational cost of high fidelity simulations such as large eddy simulations (LES) and Reynolds-averaged Navier–Stokes (RANS). In this work, the uncertain meteorological quantities viz., wind speed and its direction from field measurements are taken as inputs to RANS simulations that use realizable  $k - \epsilon$  turbulence model, to investigate their effects on passive scalar dispersion in central London. The mean wind and scalar quantities from RANS are initially validated with wind-tunnel data and compared to large eddy simulations (LES). For comparison with field measurements, the deduced probability density function (pdf) for wind speed and direction from the field are used as inputs for RANS simulations. For a 3-min averaged concentration at a specific receiver location, LES with unsteady wind inputs showed better performance than LES with mean wind input and RANS whereas for 30-min averaged concentration at various receiver locations, performance measures indicated that RANS is better than LES. The latter certainly suggests the importance of considering such uncertainties. The flow variability in every street is quantified using RANS simulations. This demonstrated that approximations used in a fast, low-order street network model may not be necessarily valid for every street of heterogeneous urban canopies, which in turn affects scalar prediction.

**Keywords** DAPPLE · Dakota · Large eddy simulation · Reynolds-averaged Navier–Stokes · SIRANE · Wind-tunnel

## List of symbols

$C$  Concentration of scalar

---

Vinh-Tan Nguyen, Daniel J. Wise and Jason Yu Chuan Leong have equally contributed to this work.

---

Bharathi Boppana  
boppanavbl@ihpc.a-star.edu.sg

Extended author information available on the last page of the article

---

$C^*$	Normalised scalar concentration
$h$	Building height
$h_m$	Mean building height
$k$	Turbulent kinetic energy
$k_m$	Molecular diffusivity
$k_t$	Turbulent diffusivity
$M_\ell$	Reference mesh where $\ell = 0, 1, 2$ in increasing order of mesh resolution
$\mathcal{N}$	Sample size
$p$	Pressure
$Q_S$	Volumetric source
$R_n$	Receiver locations
$s$	Street index
$S_m$	Source locations
$Sc_m$	Molecular Schmidt number
$Sc_t$	Turbulent Schmidt number
$t$	Time
$\mathbf{u}$	Velocity magnitude
$u_*$	Surface friction velocity
$u_d$	Bulk exchange mass velocity
$\mathbf{u}_{BT}$	$\mathbf{u}$ at BT tower height
$\mathbf{u}_{hm}$	$\mathbf{u}$ at mean building height
$\mathbf{u}_{ref}$	$\mathbf{u}$ at reference height
$\mathbf{u}_s$	Street channel velocity
$\mathbf{u}_{zmax}$	$\mathbf{u}$ at free stream height
$\mathcal{V}_s$	Volume of street canyon, $s$
$z$	Vertical coordinate or height from ground
$z_0$	Aerodynamic roughness length
$\epsilon$	Mesh convergence error
$\varepsilon$	Turbulence dissipation rate
$\kappa$	Von Karman constant
$\nu$	Kinematic viscosity
$\nu_t$	Turbulent viscosity
$\rho$	Density
$\sigma_w$	Standard deviation of the vertical velocity at roof level
$\sigma_{\phi_s}$	Standard deviation of $\langle \phi \rangle_s$ from $\bar{\phi}_s$
$\xi_s$	Standard deviation of velocity magnitude in street $s$
$\phi_s$	Velocity component of street, $s$ where $\phi = u, v, w$
$\bar{\xi}_s$	Ensemble average of $\xi_s$
$\langle \phi \rangle_s$	Volume average of $\phi_s$
$\underline{\phi}_s$	Ensemble average of $\phi_s$
$\omega$	Specific dissipation rate

## Abbreviations

ANOVA	Analysis of variance
BT	British Telecom
CFD	Computational fluid dynamics
CI	Confidence interval
ClearfLo	Clean Air for London

DNS	Direct numerical simulations
LBM	Lattice Boltzmann method
LES	Large eddy simulations
LiDAR	Light Detection and Ranging
MRI	Magnetic resonance imaging
NAD	Normalised absolute difference
NMSE	Normalised mean square error
pdf	Probability density function
POD	Proper orthogonal decomposition
QoI	Quantities of interest
RANS	Reynolds-Averaged Navier–Stokes
SDG	Sustainable Development Goals
UQ	Uncertainty quantification
VLES	Very large eddy simulations
WCC	Westminster City Council
AERMOD	American Meteorological Society/Environmental Protection Agency Regulatory Model
CALPUFF	California puff model
Dakota	Design Analysis Kit for Optimization and Terascale Applications
DAPPLE	Dispersion of air pollution and its penetration into the local environment
EPSRC	Engineering and physical sciences research council
QUIC	Quick Urban and Industrial Complex

## 1 Introduction

Good health and well-being, as well as sustainable cities and communities, are two out of 17 Sustainable Development Goals (SDG) set by the United Nations that emphasise improving air quality to achieve the targets by 2030 [36]. Owing to the complex urban form and its rapidly changing dynamics due to economic demands, pollution transport in urban areas is always proven to be challenging for both experiments and modelling communities alike. In addition to air quality, the prediction of chemical transport from any hazardous release in an urban area is of utmost importance for emergency evacuation measures. There exists a substantial amount of literature on various methods of modelling and measuring urban pollution and hazardous chemical release and how such releases impact urban environments. For instance AERMOD—plume model [9] and CALPUFF—puff model [28] are widely used for regulatory purposes by U.S Environmental Protection Agency; measurements include water-flume experiments with Planar Laser-Induced Fluorescence [21] and MRI (magnetic resonance imaging) techniques [29]; measurements in field campaigns such as ClearLo—Clean Air for London [6] include using various types of instruments to measure pollutants such as particulate matter,  $\text{CO}_2$ ,  $\text{CH}_4$  etc.; Computational Fluid Dynamic (CFD) models include direct numerical simulations (DNS), LES and RANS approach depending on the computational resources and accuracy. Whilst many of the modelling and laboratory experiments have shed light on various aspects of scalar (either pollution or hazardous release) transport, a very few computational studies (e.g., [10, 13, 24]) considered the uncertainties associated with the inputs to the model and relevant details of these studies are provided in following paragraphs.

Many CFD studies stated wind-direction and other parameters could provide more insights into ventilation and dispersion patterns but could not be considered because of computational and other constraints (e.g., [18]). This emphasises the importance of considering some of those input parameters in the model instead of using a single input for wind. Jurado et al. [19] performed 126 RANS simulations by considering 18 wind directions and seven urban configurations that included real building and road layouts from Strasbourg city to calculate the mean annual concentration obtained from a passive scalar release on the road surface. They observed that simulations from one wind direction out of two for every  $20^\circ$  step in wind rose, an overall error in predicting mean annual concentration is 13.8% for a calculation gain of 50%. When the predominant direction approach is considered, simulations from the first twelve wind directions resulted in an overall error of 10% for a calculation gain of 35%. This is an important finding as most studies limit to predominant wind directions, mainly due to computational constraints. By considering seven inlet wind directions within a  $30^\circ$  sector in RANS computations, Wise et al. [40] showed major changes in the simulated flow patterns among buildings in Singapore. This shows that even when predominant wind directions are considered, a small change in approaching wind direction could affect the ventilation rate remarkably.

As stated earlier, only very few studies considered more than one uncertainty associated with the inputs to the model. In their DNS study, Coceal et al. [10] varied approaching wind-direction, building layout and source location. Given that DNS can resolve all the turbulent scales of a flow field, the findings are very useful in understanding near-field dispersion. However, the geometry comprises a regular array of cubical obstacles. Margheri and Sagaut [24] used hybrid anchored-ANOVA (analysis of variance)—POD (proper orthogonal decomposition)—Kriging method—a first such uncertainty quantification (UQ) approach for toxic gas dispersion in Shinjuku area of  $1 \text{ km}^2$  located in Tokyo, Japan. The simulations are performed using Lattice Boltzmann method—Very Large Eddy Simulations (LBM-VLES) and focused on assessing uncertainties (wind speed, wind direction, position and diameter of source) on quantities of interest (QoI) on a horizontal plane. While this study shows the potential of the UQ approach using high-fidelity simulations for such complex flows, no comparison with field or wind-tunnel measurements is performed. The importance of considering meteorological uncertainty for scalar dispersion and source estimation in urban areas was demonstrated by Lucas et al. [23] by comparing their RANS simulation data with field measurements from the Joint Urban 2003 campaign in Oklahoma City. The authors used a data-driven Bayesian approach to estimate the uncertainty. Three uncertain input parameters (wind speed, wind direction and upstream terrain roughness height) are considered by García-Sánchez et al. [13] in their UQ approach to predict scalar dispersion in downtown Oklahoma City. The wind speed and wind direction were obtained from the Joint Urban 2003 field campaign. The authors compared the mean and 95% CI of the scalar to the field measurements, thereby showing the sensitivity of the inlet parameters to the prediction at various locations. García-Sánchez and Gorlé [12] used an ensemble of mesoscale simulations as inputs for CFD to quantify the effect of uncertainties in inflow boundary conditions on wind and concentration prediction in the region of interest. They showed that such an approach can be an alternative if field measurements are not available. The field measurements are generally obtained using anemometers or remote sensing devices such as LiDAR whose applications in numerical models are recently reviewed by Liu et al. [22]. For simulations with uncertain inputs, the RANS modelling approach is generally feasible as they take relatively less computational resources and time than LES even though the latter can accurately predict complex interaction of turbulent flow

structures and dispersion processes. There also exists fast models that require much lesser computational time and resources than RANS.

Fast models such as QUIC-URB [26] and SIRANE [30] are used to predict scalar transport when computational time and resources are very limited or for emergency planning purposes. In street network models, the complex building morphology is represented as a combination of links and nodes that depict streets and intersections. This simplification renders modelling wind flow and turbulence using parametric relations. Using mass flow balance, uniform distribution of concentration in the streets is predicted from a steady source release. The model is validated with wind-tunnel experiments [8] and field measurements [31, 34]. The unsteady version of the source release is modelled using SIRANERISK [33]. By comparing different dispersion algorithms in simulating near-road air pollution, Wang et al. [38] showed SIRANE output was sensitive to the built environment. The same street network model was evaluated by Grylls et al. [14] using the LES model in the prediction of both inert ( $\text{NO}_x$ ) and reactive pollutants (NO,  $\text{NO}_2$  and  $\text{O}_3$ ) in South Kensington, London. While the dominant trends of canyon-averaged concentrations could be captured by the street network model, predictions in short streets and those next to open spaces were found to be erroneous. Fellini et al. [11] used a complex network model inspired by SIRANE on four cities—Paris, Firenze, Lyon and New York—and showed how the topology of a city and its interaction with the approaching wind affects the dispersion of airborne releases. Such information is crucial to estimate the critical locations that are responsible for high pollution levels over a given area, especially for emergency planning scenarios. An evaluation of fast dispersion models in a regular street network by Hertwig et al. [17] show that these fast models perform well in capturing building-induced dispersion processes for regular urban topology. But such regularity is rarely the case in reality.

So, it is pertinent to ask feasibility of the RANS approach for full-scale urban simulations with uncertain meteorological inputs. Though this was addressed in earlier stated UQ studies, it was never conducted for DAPPLE—Dispersion of Air Pollution and its Penetration into the Local Environment—a field campaign in central London. The current study incorporates the meteorological uncertainty inputs in approach flow and compares them with field measurements and LES. The study also shows the performance of RANS and street network models on DAPPLE—which to the authors' knowledge was not discussed before. As this article focuses on the comparison of available point measurement data from various methods, a detailed analysis of the three-dimensional distribution of wind and scalar is not addressed.

The remaining of this paper has the following sections. Section 2 contains a description of DAPPLE geometry and numerical settings. Verification and validation of RANS are included in Sect. 3. The results from UQ of wind on scalar dispersion using RANS are discussed in Sect. 4 and lastly, Sect. 5 concludes the paper.

## 2 Geometry and numerical settings

### 2.1 About DAPPLE

The DAPPLE field site is located in Westminster, Central London. This project was initially a 4-year (2002–2006) project funded by Engineering and Physical Sciences Research Council (EPSRC) within the Infrastructure and Environment Programme with an aim to enhance understanding of pollutant dispersion processes in realistic urban environments [2]. A field campaign in central London held during these 4 years focused on human

exposure to traffic pollution and how the wind in street canyons are affected by traffic and street layout. To build a larger database that helps to evaluate modeling techniques and obtain detailed spatial and temporal variability of dispersion processes, the campaign was extended in 2007 to further include wind-tunnel simulations and computational modelling [41]. A detailed description of this site and field measurements can be obtained from [2–4, 41]. For the sake of clarity, only relevant information on the campaign is provided here.

The field site shown in Fig. 1 encompasses buildings surrounding two major busy roads—Marylebone Road and Gloucester Place. The field site axis along these two roads is tilted approximately at  $20^\circ$  anticlockwise to the geographic coordinate system. This axis forms the reference for geometry for the remainder of this paper. The plan view of this geometry along with the source  $S_m$  and receiver  $R_n$  locations of the scalar is shown in Fig. 2. Here,  $m = 2, 5$ , and  $6$ , and  $n = 1$  to  $13$ . The Marylebone road is approximately  $40\text{ m wide} \times 774\text{ m long}$  and oriented WSW-ENW. The Gloucester Pl which intersects Marylebone Road perpendicularly is approximately  $25\text{ m wide} \times 625\text{ m long}$ . The mean and maximum height of buildings is  $22\text{ m}$  and  $64\text{ m}$  respectively. All the buildings are of different sizes, thus representing the typical complexity of an urban area. For example, the Westminster City Council House, where  $R_5$  is located in Fig. 2 on the SW corner of the intersection is approximately of size  $50\text{ m} \times 35\text{ m} \times 15\text{ m}$  and has a central clock tower of diameter  $5\text{ m}$  and height  $34\text{ m}$ .

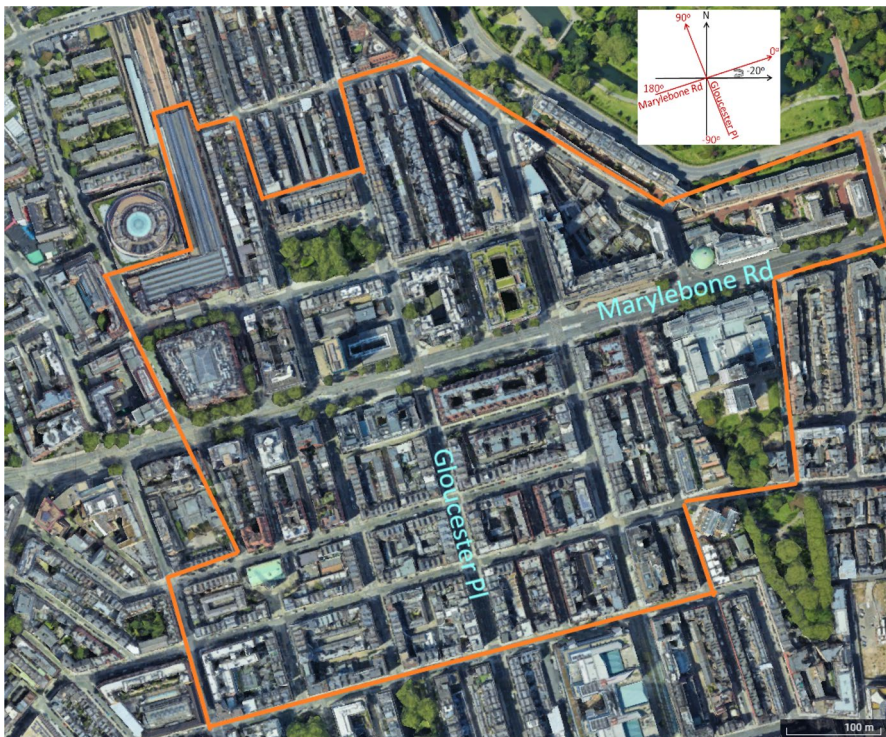


**Fig. 1** The Google Earth map showing the DAPPLE field site. Enclosed within the orange solid line is the geometry used for simulations

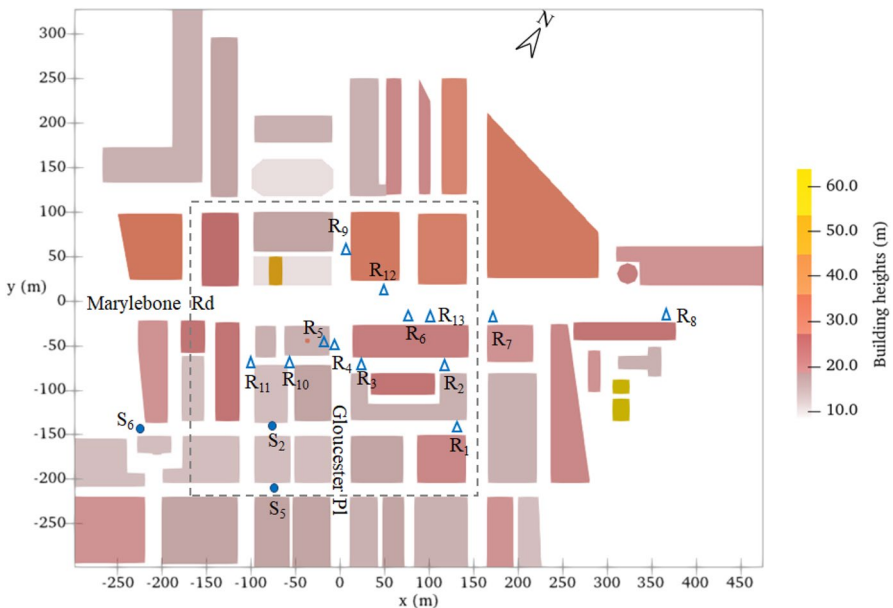


**Fig. 2** Plan view of DAPPLE geometry with source,  $S_m$  and receiver,  $R_n$  locations;  $m = 2, 5, 6$  and  $n = 1$  to 13. The coordinates of these locations are given in Table 3.  $R_5$  is located on the rooftop of Westminster City Council House. The region enclosing dashed lines is refined further for mesh convergence checks

The wind-tunnel experiments of the same campaign at a geometry scale of 1:200 are performed in the Environmental Flow wind-tunnel laboratory at the University of Surrey, U.K. The study area in the field is approximately 250–300 m in radius with the intersection of two roads at its centre, while the wind-tunnel experiments cover approximately 500 m radius to take into account the aerodynamic roughness of this site to a certain extent. A fully developed boundary layer upstream of the DAPPLE geometry was generated using Irwin spires and surface roughness mounted upwind of the model. For more details of wind-tunnel experiments, the reader may refer to Carpentieri et al. [7], hereafter referred to as ‘CRB09’.

The LES data corresponding to wind-tunnel experiments and field measurements are available from Xie and Castro [44] and Xie [42]. For ease, these are referred to as ‘XC09’ and ‘X11’ respectively in the subsequent sections of this article. The source and receiver locations are denoted differently in XC09 and X11. In order to maintain consistency, the source locations  $S_2$  and  $S_5$ , and receiver locations  $R_1$  to  $R_{10}$  are the same as defined in XC09. Continuing with this definition, the third source location is denoted as  $S_6$ , which is the same as  $X_2$  in ‘X11’. The coordinates of these source and receiver locations are given in Table 3.

## 2.2 Numerical settings

### 2.2.1 Computational domain and mesh

The computational domain is of size 3200 m  $\times$  3200 m  $\times$  220 m containing the buildings’ bounding box of 775 m  $\times$  625 m  $\times$  64 m; this ensures sufficient fetch in the horizontal domain

for the wind to approach in any direction. A 3D view of the computational domain with buildings and surface mesh is shown in Fig. 3a. In order to show the buildings clearly, the bounding box in this figure is not the actual scale that is used in simulations. The OpenFOAM built-in meshing tool snappyHexMeshDict with snap features is used to generate hexahedral-dominated mesh for simulations. The mesh resolution is controlled by a background mesh resolution in horizontal and vertical planes as well as the number of refinement levels. A section of y-plane of the computational mesh is shown in Fig. 3b illustrating varying mesh resolution across the domain.

### 2.2.2 Governing equations

The three-dimensional, steady, incompressible RANS equations in Einstein notation are:

$$\frac{\partial u_j}{\partial x_j} = 0, \quad (1)$$

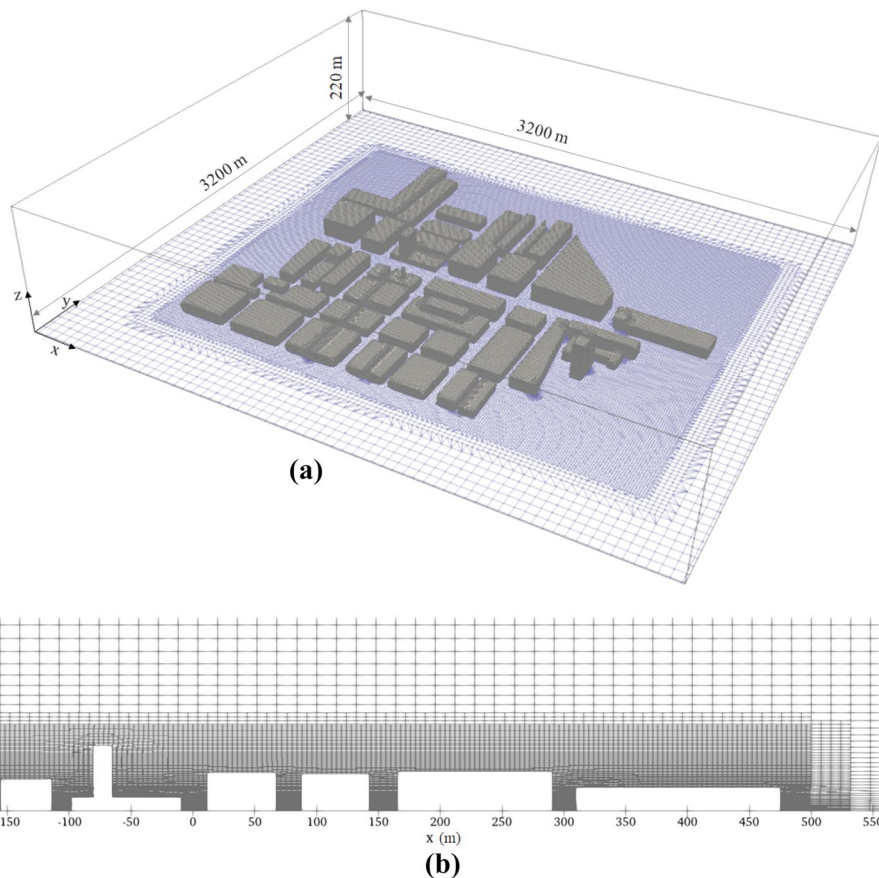


**Fig. 3** **a** Computational domain (not to scale) with surface mesh on the bottom boundary and buildings, and **b** a section of y-plane showing varying mesh resolution

$$u_j \frac{\partial u_i}{\partial x_j} = -\frac{1}{\rho} \frac{\partial p}{\partial x_i} + \nu \frac{\partial^2 u_i}{\partial x_j \partial x_j} - \frac{1}{\rho} \frac{\partial u_i u_j}{\partial x_j}, \quad (2)$$

where  $x_i$  are three cartesian coordinates,  $u_i$  are time-averaged velocity components in  $i$ th direction,  $p$  is pressure,  $\rho$  is density,  $\nu$  is kinematic viscosity and  $u_i u_j$  is Reynolds stress tensor which is modelled using linear eddy viscosity hypothesis given as:

$$u_i u_j = \frac{2}{3} k \delta_{ij} - 2 \nu_t S_{ij}, \quad (3)$$

where  $k$  is turbulent kinetic energy,  $\delta_{ij}$  is Kronecker delta,  $S_{ij}$  is time-averaged strain tensor and  $\nu_t$  is turbulent viscosity.

To model the turbulence, the realizable  $k - \varepsilon$  model is used whose governing equations for turbulent kinetic energy  $k$  and turbulent dissipation rate  $\varepsilon$  are:

$$u_j \frac{\partial k}{\partial x_j} = \frac{\partial}{\partial x_j} \left[ (\nu + \nu_t) \frac{\partial k}{\partial x_j} \right] + P_k - \varepsilon, \quad (4)$$

$$u_j \frac{\partial \varepsilon}{\partial x_j} = \frac{\partial}{\partial x_j} \left[ (\nu + \frac{\nu_t}{\sigma_\varepsilon} \frac{\partial \varepsilon}{\partial x_j}) \right] + C_1 S \varepsilon - C_2 \frac{\varepsilon^2}{k + \sqrt{\nu \varepsilon}}, \quad (5)$$

where  $P_k$  is the turbulent production,  $S = \sqrt{2S_{ij}S_{ij}}$  and model constants are  $\sigma_k = 1$ ,  $\sigma_\varepsilon = 1.2$  and  $C_2 = 1.9$ .  $C_1$  and  $\nu_t$  are defined as:

$$C_1 = \max \left( \frac{\eta}{5 + \eta}, 0.43 \right), \quad \eta = S \frac{k}{\varepsilon}, \quad (6)$$

$$\text{and} \quad \nu_t = C_\mu \frac{k^2}{\varepsilon}, \quad C_\mu = \frac{1}{A_0 + A_s \frac{k U_*}{\varepsilon}}, \quad (7)$$

where  $A_0 = 4$  [25]. This turbulence model is also used for similar dispersion studies by Blocken et al. [5], Keshavarzian et al. [20] etc. By comparing to wind-tunnel measurements, it was shown by Ricci et al. [27] that standard and realizable  $k - \varepsilon$  models are generally better in modelling urban wind than other turbulence models.

The governing equation for passive scalar transport is given by

$$\frac{\partial C}{\partial t} + \frac{\partial(u_j C)}{\partial x_j} = \frac{\partial}{\partial x_j} \left( (k_m + k_t) \frac{\partial C}{\partial x_j} \right) + S, \quad (8)$$

where  $C$  is concentration of passive scalar,  $k_m$  and  $k_t$  are molecular and turbulent diffusivity respectively and  $S$  is source term.  $k_m = \nu / Sc_m$  and  $k_t = \nu_t / Sc_t$ , where  $Sc_m$  and  $Sc_t$  are molecular and turbulent Schmidt numbers. Earlier studies (e.g. [13, 35, 44]) used Schmidt number values ranging from 0.7 to 1.0 in their computations. There exists no general of thumb on what values should be exactly used and therefore we chose  $Sc_m = 0.7$  and  $Sc_t = 0.9$  which are commonly used in literature. A volumetric source,  $Q_S$  is released at three source locations— $S_2$ ,  $S_5$ , and  $S_6$  and are shown in Fig. 2. The scalar is released after the flow is fully converged to simplify the computational process. For comparison purposes, the resulting scalar,  $C$  is normalised as

$$C^* = \frac{C_{\text{u}_{\text{ref}}} h_m^2}{Q_s}, \quad (9)$$

where  $\mathbf{u}_{\text{ref}}$  is wind speed at free stream height in Sect. 3.2 and denoted as  $\mathbf{u}_{z_{\max}}$ , at BT tower height in Sect. 4.2 and denoted as  $\mathbf{u}_{BT}$ , and at mean building height,  $h_m$  in Sect. 4.3 and denoted as  $\mathbf{u}_{hm}$ . This is in accordance with the literature data used for comparison.

### 2.2.3 Boundary conditions and solver settings

The atmospheric boundary layer profiles are specified at the inlet boundaries for velocity  $\mathbf{u}$ , turbulent kinetic energy  $k$ , and turbulent dissipation  $\varepsilon$  and are given as:

$$\mathbf{u} = \frac{u_*}{\kappa} \ln\left(\frac{z + z_0}{z_0}\right), \quad (10)$$

$$k = \frac{u_*^2}{\sqrt{C_\mu}}, \quad (11)$$

$$\varepsilon = \frac{u_*^3}{\kappa(z + z_0)}, \quad (12)$$

where  $\kappa = 0.41$  is the von Karman constant,  $u_*$  is the friction velocity,  $z$  is height from ground and  $z_0$  is the aerodynamic roughness length. Using the information of reference wind speed at a specific height from wind-tunnel or field data,  $u_*$  can be obtained using Eq. (10). The value of  $z_0$  is specified as 1 m, as per Davenport's classification given by Wieringa [39] for rough built-up terrain. A slip boundary condition is imposed on the top surface and zero static pressure is specified on outlet boundaries. The ground and building surfaces are considered as rough surfaces and specified with wall functions consistent with atmospheric boundary layer [16].

The semi-implicit method for pressure-linked equations (SIMPLE) is used for pressure–velocity coupling to solve the incompressible Navier–Stokes equations. The bounded second-order schemes for momentum and scalar and hybrid schemes for turbulence are used for discretization. A residual control of  $10^{-4}$  is specified for all the governing variables. All the simulations are carried out using the open-source software version 2012 OpenFOAM [25].

## 3 Verification and validation

### 3.1 Verification: mesh sensitivity

Three mesh sizes are used for mesh sensitivity checks. The horizontal mesh resolution varies from 1.25 m in the narrow gaps to 5 m in the wider gaps of buildings for coarse mesh; from 1 m in the narrow gaps to 4 m in the wider gaps of buildings for medium mesh. For fine mesh, a region bounded by the dashed line in Fig. 2 and up to mean building height is further refined from the medium mesh to double the mesh resolution. For all the meshes, the horizontal mesh resolution in the buildings' region is twice finer as in the remaining

**Table 1** Details of the meshes considered in sensitivity study and the convergence error

Mesh	$\Delta x/h_m = \Delta y/h_m$	$\Delta z/h_m$	Total cell count (mil)	$\epsilon(\mathbf{u})$	$\epsilon(k)$
$M_0$	0.057–0.227	0.009–0.032	3.7	0.1217	0.1444
$M_1$	0.045–0.182	0.009–0.032	5.1	0.0751	0.0594
$M_2$	0.023–0.091	0.004–0.016	6.4	0.0000	0.0000

As the mesh is non-uniform, minimum and maximum resolution is shown within the buildings' region and up to mean building height

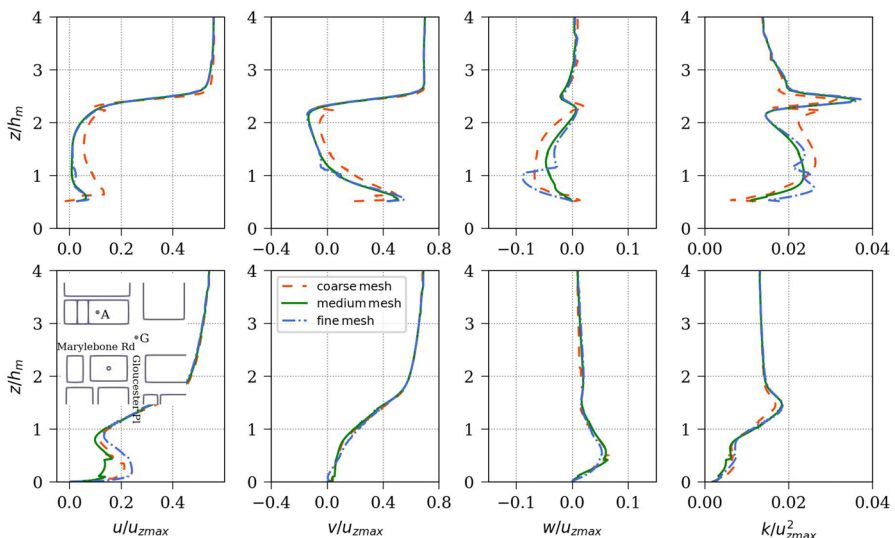


**Fig. 4** Comparison of normalized vertical profiles of velocity components and turbulent kinetic energy at 'A' (top row) and 'G' (bottom row) from three mesh resolutions— $M_0$ ,  $M_1$  and  $M_2$  whose details are given in Table 1

part of the computational domain. It is suggested by Xie and Castro [43] that at least 15–20 mesh points per building dimension are sufficient for simulating large-scale flow dynamics of an urban area. In Xie and Castro [44], 1 m resolution was used to resolve the flow around buildings. For the current RANS computations, within the buildings' region, successive cells in vertical direction follow a geometric ratio such that the resolution is 0.2 m near the ground and 1.5 m at 75 m height—this resulted in approximately 55 mesh points per mean building height for coarse and medium meshes and 110 mesh points per mean building height for fine mesh. In total, the coarse, medium, and fine mesh consists of approximately 3.7 million, 5.1 million, and 6.4 million cells respectively as shown in Table 1.

For these three meshes, the simulations are performed with an approaching wind direction of  $-51.35^\circ$  in model coordinates (see inset in Fig. 1) and the reference wind speed of 5 m/s at 22 m height. A comparison of the flow field for all the mesh resolutions is shown in Fig. 4 for two selected locations. At 'A', which is above a building as shown in the 'inset' of this figure, the non-dimensional flow statistics are visibly identical between medium and fine mesh except for some difference in vertical velocity  $w$  and turbulent kinetic energy  $k$

below  $z/h_m = 2$ . Likewise, at intersection ‘G’, except for differences in  $u$  below  $z/h_m = 1$ , the profiles of the remaining flow statistics are identical between the fine and medium mesh. The flow statistics for coarse mesh notably differ with fine and medium meshes at ‘A’, but closely match at ‘G’. Since the mesh is non-uniform and not exactly a factor of two for coarse, medium, and fine meshes, the mesh convergence error is defined as the mean of  $L_2$  norm of error between meshes as given in Eq. (13).

$$\epsilon(\alpha) = \frac{1}{N_{loc}} \sum_{loc} \frac{\|\alpha_{M_\ell} - \alpha_{M_2}\|_{loc}}{\|\alpha_{M_2}\|_{loc}}, \quad (13)$$

where ‘loc’ is ‘A’ and ‘G’,  $N_{loc}$  is the number of locations,  $\alpha$  is velocity magnitude  $\mathbf{u}$  and  $k$ ,  $M_\ell$  is  $M_0$ —coarse mesh,  $M_1$  - medium mesh and  $M_2$ —fine mesh. From Table 1, it can be observed that the error from medium mesh is very small and also lower than coarse mesh. Hence, medium mesh resolution is chosen for subsequent simulations.

### 3.2 Comparison of the flow field and mean scalar from RANS with wind-tunnel experiments and LES

Results from the above medium mesh RANS simulation are compared with LES (XC09) and validated with wind-tunnel experiments (CRB09). Figure 5 shows the comparison of normalised velocity and turbulent kinetic energy profiles at three unique locations—‘A’ is above a building rooftop, ‘G’ is at the intersection, and ‘T’ is along one of the main roads, away from the intersection. For LES, information was only available at ‘G’ in XC09. Here, the flow statistics are normalised with the free stream conditions prescribed at the top of the inlet.

Upon comparing flow statistics from three methodologies, a few notable observations are:

- (a) The streamwise velocity,  $u$  near the ground agrees with wind-tunnel experiments, whereas LES at the intersection ‘G’ differs from both wind-tunnel and RANS.
- (b) A qualitative agreement is observed for  $w$  whose values are usually lower than  $u$  and  $v$ .
- (c) The turbulent kinetic energy from RANS is under-predicted below  $z/h_m \approx 2.5$  while LES over-predicted below  $z/h_m \approx 1$ .

As LES data is available at ‘G’, the difference in normalized velocity magnitude and turbulent kinetic energy from RANS and LES to wind-tunnel are calculated and shown in Fig. 6. Both RANS and LES show differences from wind-tunnel below  $z/h_m \approx 2$ . However, these differences are of  $\mathcal{O}(10^{-1})$  for normalized  $\mathbf{u}$  and  $\mathcal{O}(10^{-2})$  for normalized  $k$ . It is interesting to note that below  $z/h_m \approx 1$ , RANS under-predicted while LES is over-predicted for both  $\mathbf{u}$  and  $k$ . The differences tend to become smaller with increasing height. Having observed similar order of performance by both RANS and LES for the flow field, the next step is to compare the scalar field from these three methodologies.

The wind-tunnel and LES data on scalar dispersion are available in XC09 for two source release locations— $S_2$  and  $S_5$ —shown in Fig. 2. The duration and quantity of scalar release are not provided in these references. So, a steady continuous release of a constant volume flow rate of  $80 \mu\text{g}/\text{m}^3$  is specified in Eq. (8) to compute passive scalar transport. Figure 7

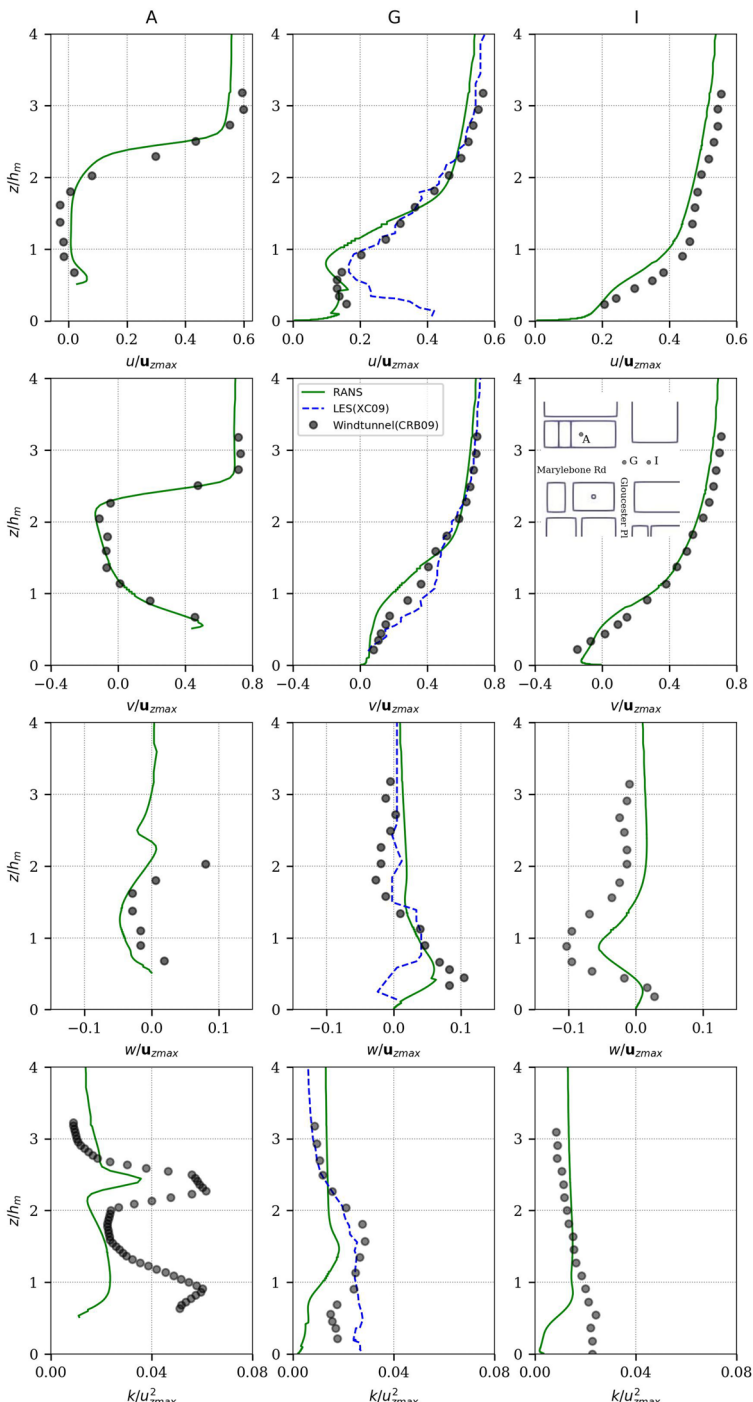


**Fig. 5** Comparison of normalized vertical profiles of velocity components and turbulent kinetic energy at three locations

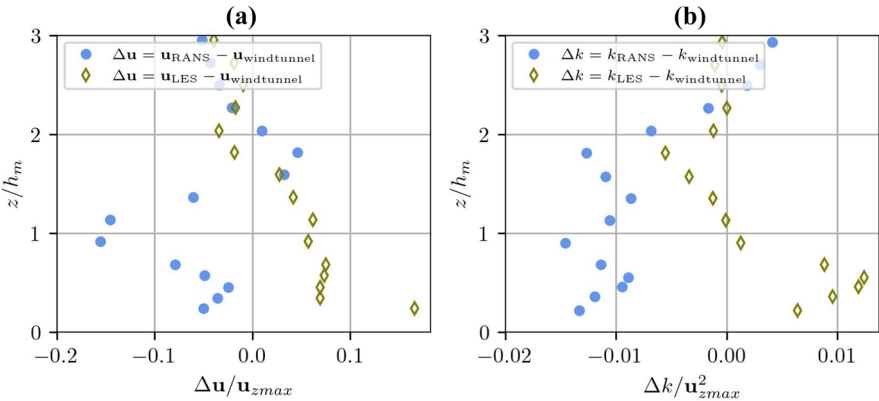


**Fig. 6** Normalized difference in vertical profiles of velocity magnitude and turbulent kinetic energy at location ‘G’ between RANS and LES to wind tunnel data. The position of ‘G’ is shown in the inset of Fig. 5

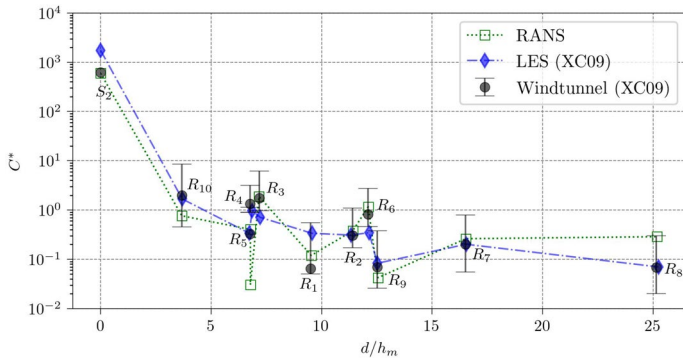


**Fig. 7** Comparison of normalized scalar at various receiver locations corresponding to source release at  $S_2$ .  $d = |X_R - X_S| + |Y_R - Y_S|$ , where  $(X_R, Y_R)$  are the coordinates at receiver locations and  $(X_S, Y_S)$  are the coordinates at source location,  $S_2$

compares normalized concentrations (Eq. 9) at several receiver locations corresponding to source release at  $S_2$ . Except for  $R_4$  and  $R_5$ , 80% of RANS data lies within the standard deviation of wind-tunnel data at all receiver locations. It is remarkable to note that the current RANS results are also comparable with LES prediction across all receiver locations in comparison to the wind-tunnel data.

Figure 8 shows normalized concentrations along Marylebone Road corresponding to source release at  $S_5$ . Similar to wind-tunnel and LES, the two prominent scalar peaks are predicted in RANS, but the first peak in RANS is nearly twice larger than LES and wind-tunnel. Also, the secondary peak from RANS is lower than experiments by 0.02 and shifted to the right by  $\Delta x/h_m = 1.5$ . This shift in the second peak is similarly observed in the LES prediction; however, the present RANS result shows a second peak closer in magnitude to the experiment data than the reference LES data. Both the RANS and LES results fail to capture the sharp drop in concentration as observed in experiments at  $x/h_m = 10$ .

The comparison of RANS versus wind-tunnel experiment data and LES shows its promising performance in the prediction of flow statistics and especially scalar transport in an

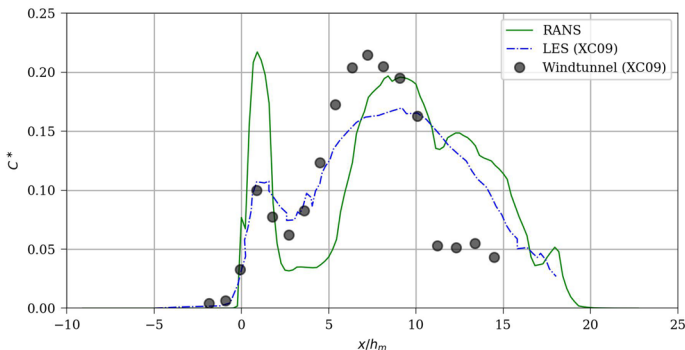


**Fig. 8** Comparison of normalized scalar at  $z/h_m = 0.127$  along Marylebone Road corresponding to source release at  $S_5$

urban environment. Under-prediction of the RANS model for turbulence kinetic energy in the building canopy highlights its inherent limitations in turbulence modelling compared to LES with more resolving time and spatial scale capability. Perhaps, it is possible to address this limitation using machine learning approaches by fine-tuning the RANS turbulence model coefficients as shown by Volpiani et al. [37]. In this study, we focus on using the conventional turbulence model. Despite its shortcomings, the current RANS's performance for scalar dispersion provides a favourable and efficient alternative for large-scale study in an urban environment primarily on the balance of computational time versus accuracy. The question then is how does the current methodology perform on a field test where there are many input uncertainties, the predominant being wind speed, and direction? Do the uncertain inputs result in severe under- or over-prediction of the scalar? These questions are addressed in the following section.

## 4 Uncertainty quantification of wind conditions on scalar dispersion using RANS

### 4.1 Input uncertainties for scalar dispersion in field

It is known that the wind speed and direction are highly unsteady in urban areas; thus generating uncertainties in input conditions to numerical simulations. The uncertainties in these two variables are taken into account in the current RANS computations by varying wind speed and direction at the inlet boundary of the computational domain. These uncertain inputs are obtained by deducing the information provided in Wood et al. [41] and Balogun et al. [3] whose details are given below.

In the field experiments, wind speed and its direction were recorded by a mast on the rooftop of Westminster City Council (WCC) library shown in Fig. 2 for 5 weeks duration at 20 Hz. The probability density function of 15-min mean of this data was provided in Balogun et al. [3]. Since the approach flow inputs have to be outside the DAPPLE site for RANS, the information on wind is deduced from the correlation between measurements obtained from British Telecom (BT) tower and WCC provided in Wood et al. [41]. The correlation for 15- min mean wind speeds and wind direction is available for the whole year 2007. The BT tower is approximately located 1500 m east of the DAPPLE site and

the measurements were obtained from ultrasonic anemometers mounted on a lattice mast at 190 m height above street level. From the correlation scattergram plots, it is inferred that the wind speed on the WCC rooftop is a factor of 4.1 slower, and the wind direction veers with the height from rooftop to tower top by a mean angle of 9°. These factors are taken into account to deduce the probability density function (pdf) of wind speed and direction at BT tower using the pdf of data measured at the WCC rooftop. The resulting pdf is shown in Fig. 9. In the case of wind speed, Fig. 9a shows a distribution with positive skewness whereas pdf of wind direction in Fig. 9b exhibits trimodal distribution with the first peak approximately 2.2 times larger than the two peaks.

Forward propagation of inlet uncertainties is one of the approaches to quantify their effects on QoI, which is the scalar prediction in the current study. This is achieved by using Dakota [1], open-source software for large-scale engineering optimization and uncertainty analysis. In general, uncertainties are broadly classified as aleatory, which is irreducible, and epistemic, which is due to a lack of knowledge. The latter is largely due to turbulence modelling in RANS and the former is due to the inherent nature of the system. As we are focusing only on aleatory uncertainties, there are two sampling methods available in Dakota—Monte Carlo and Latin hypercube. The latter sampling approach is used in this study as it generally requires fewer samples than Monte Carlo for obtaining the same accuracy in statistics [1]. We used 100 Latin hypercube samples that adequately represent the deduced pdf of wind speed and direction and are shown in Fig. 10. This implies that 100 RANS computations are performed to propagate the inlet uncertainties for scalar prediction. The mean and 95% CI of scalar from these 100 computations are compared with LES and field measurements.

## 4.2 Comparison of mean scalar from RANS with field experiments and LES

The flow field is initially simulated using the steady-state RANS approach. The converged flow field is used as an input to transient simulations of passive scalar dispersion according to Eq. (8). In the field, the scalar at  $S_6$  is released for 15 min. As the information on the quantity of scalar release at the source is not provided in Xie [42], a volumetric source of  $80 \mu\text{g}/\text{m}^3$  is released for 15 min and stopped for the remaining 15 min. The resulting concentration values are normalized using Eq. (9).

The 3-minute time average of the scalar at the receiver location  $R_4$  during and post-release of the scalar are compared with LES and field data in Fig. 11. The LES and field

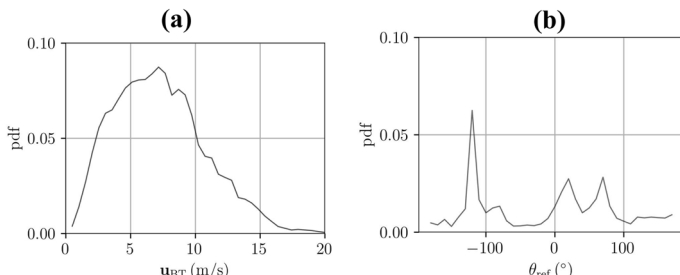


**Fig. 9** The probability density function of **a** wind speed and **b** wind direction on top the BT tower deduced from measurement at the rooftop of the WCC building. The measured data is obtained from the earlier work of Balogun et al. [3]

**Fig. 10** Scatter plot of 100 samples of wind speed and direction used as an inlet boundary condition in the current numerical simulations. The sampling is performed with LHS taking the distribution of wind speed and direction shown in Fig. 9

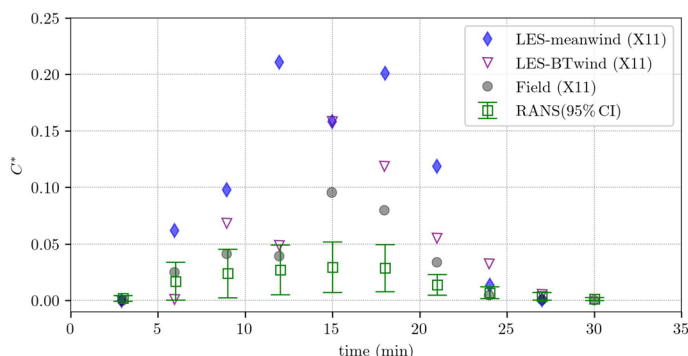
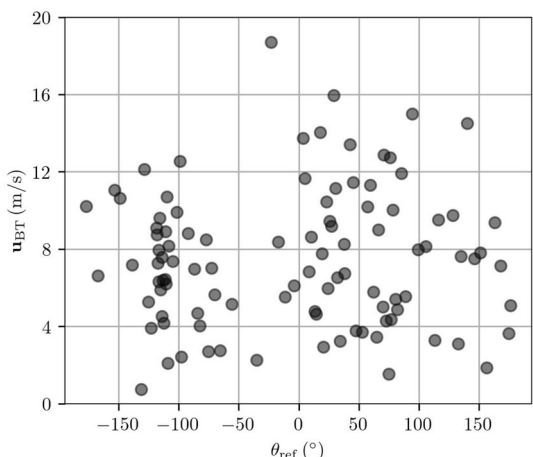


**Fig. 11** Comparison of normalized time-averaged concentration at receiver location  $R_4$  corresponding to source  $S_6$

data are obtained from Xie [42]. The LES-meanwind (X11) corresponds to simulations where the mean of wind speed and direction measured at BT tower data from 1630 to 1700 hrs is used for the inflow generation whereas LES-BTwind (X11) corresponds to the simulation with inflow generated using unsteady BT tower data. The RANS data is shown with the mean and 95% CI obtained from 100 simulations. The qualitative trend predicted by RANS is similar to field and LES. Except for time = 15th, 18th and 21st min, the RANS prediction with its 95% CI bounds is in good agreement with field measurements. These times correspond to instances where the mean scalar is at or near the maximum value. The under-prediction of RANS is expected because of its inherent limitation in the correct prediction of turbulence as stated in the last paragraph of Sect. 3.2. We observe that 60% of RANS with its 95% CI agrees with field measurements at this receiver location unlike LES with mean wind input and BT wind input that shows 22% agreement.

Figure 12 shows the variation of 30-minute averaged concentration at a few receiver locations with distance from source  $S_6$ . It is expected that the concentration of the scalar decreases with increasing distance from the source. It can be seen that the RANS prediction of mean concentration agrees well with the field measurement across all receiver

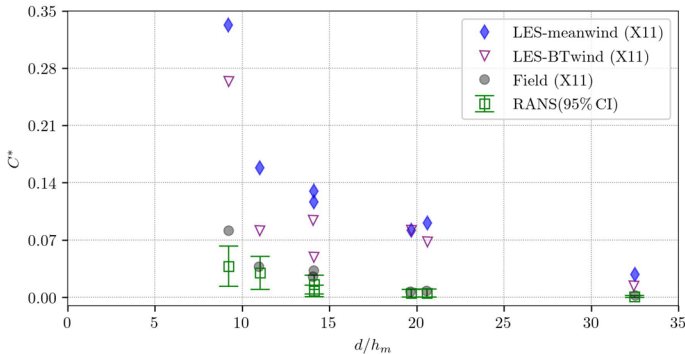


**Fig. 12** Comparison of normalized concentration at receiver locations corresponding to source  $S_6$ . The distance from source  $d = |X_R - X_S| + |Y_R - Y_S|$ , where  $(X_R, Y_R)$  are the coordinates at receiver locations and  $(X_S, Y_S)$  are the coordinates at source location  $S_6$

locations, except the closest one to the source. Furthermore, the field data is mostly within the RANS 95% CI bounds. We observe 57% of RANS data is in agreement with field data, unlike LES that consistently over-predicted, regardless of inlet conditions.

The normalised absolute difference (NAD) and the normalised mean square error (NMSE) as given in Hanna and Chang [15] are calculated to quantify the differences of mean scalar between simulations and measurements using Eqs. (14) and (15) respectively.

$$NAD = \frac{\overline{|C_o^* - C_p^*|}}{\overline{C_o^*} + \overline{C_p^*}} \quad (14)$$

$$\text{and } NMSE = \frac{\overline{(C_o^* - C_p^*)^2}}{\overline{C_o^*} \times \overline{C_p^*}}. \quad (15)$$

Here,  $C_o^*$  and  $C_p^*$  correspond to normalized concentrations from field observations and simulations respectively, and the overbar represents the average of data.

The performance measures for the data shown in Figs. 11 and 12 are given in Table 2. For 3-min averaged concentration at  $R_4$ , we observe that both NAD and NMSE from LES-meanwind (X11) are larger than RANS and LES-BTwind (X11), whereas LES-BTwind performance is better. It would be useful if such a 3-minute time average information is available at more than one receiver location to observe the repeatability of performance

**Table 2** Performance measures for different types of simulations

Data source	Simulation type	NAD	NMSE
Data from 3-min averaged concentration at $R_4$ shown in Fig. 11	RANS	0.383	1.584
	LES-meanwind (X11)	0.458	1.941
	LES-BTwind (X11)	0.266	0.462
Data from 30-min averaged concentration shown in Fig. 12	RANS	0.393	1.132
	LES-meanwind (X11)	0.656	4.141
	LES-BTwind (X11)	0.540	2.708

behavior. For a 30-min time average of concentration at various receiver locations, we observe that the performance of RANS that considered inlet uncertainties is better. Generally, LES is found to be in good agreement with wind-tunnel measurements as observed in Figs. 7 and 8. This may suggest that for a 30-min average concentration, even though unsteady inputs are used for inflow in LES, RANS demonstrated that considering the broad range of uncertainty in wind speed and direction yields better prediction.

As shown in Sect. 3.2 that RANS prediction of wind and scalar are comparable to LES and wind-tunnel measurements. When a broad range of wind speed and directions from field measurements are considered as inputs to RANS, its performance in scalar prediction is found to be better than high-fidelity LES. This may most likely suggest that uncertainties of approaching wind are significant in scalar dispersion. Therefore, it is important to consider input uncertainties for such flows to predict mean quantities of variables of interest. The question may then arise if low-order models are sufficient as they are much faster in comparison to RANS. This is addressed in the next section.

### 4.3 Comparison of mean scalar from RANS with street network model, wind-tunnel experiments and LES

The street network models are very useful for detecting the extent of scalar dispersion through faster means. In emergency scenarios especially, such models enable informed decision-making processes faster as they take into account the complexity of street networks and prevailing meteorological variables. However, these models are based on some assumptions that are not necessarily valid under all prevailing meteorological or urban topographical conditions. In this paper, we consider SIRANE, a street network model for transport and dispersion of pollutants in urban areas [30].

Carpentieri et al. [8] applied street network model for scalar dispersion study of DAPPLE. Similar to Carpentieri et al. [8], Fig. 13 shows the details of street connectivity in the building region. A comparison of normalised concentration obtained from RANS, LES, SIRANE, and wind-tunnel data for source release at  $S_2$  is shown in Fig. 14. As defined in Carpentieri et al. [8], the reference velocity is taken as the wind speed at mean building height in the approach flow to obtain  $C^*$ .

We observe that 64% of data from LES and RANS is within the bounds of two-factor prediction of wind-tunnel data while SIRANE shows that most of its data are outside the two-factor bounds. In fact, only 33% of SIRANE prediction is within two-factor bounds and large over-prediction of scalar concentration compared to measurement data can be observed. It is believed that the conservative prediction from the street network model is caused by some of its inherent assumptions or approximations. For instance, the bulk mass exchange velocity used to compute turbulent mass fluxes at the roof level is defined as [32]

$$u_d = \frac{u_*}{\pi\sqrt{2}} = \frac{\sigma_w}{\pi\sqrt{2}} \quad (16)$$

Here  $u_*$  is the surface friction velocity and  $\sigma_w$  is the standard deviation of the vertical velocity at roof level. This is proven to be sufficient for a square street canyon of infinite length. But for streets of finite length, the flow topology is complex and as a result, a single representation of Eq. (16) may not be necessarily valid always. In SIRANE, the dependence of  $u_d$  on approach flow direction and street aspect ratios are neglected in a first approximation. Though the wind-tunnel experiment has a fixed direction for the approach flow, street

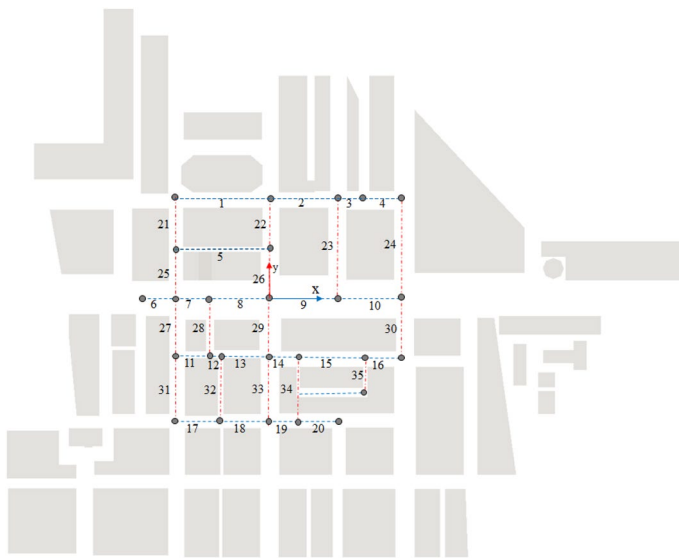
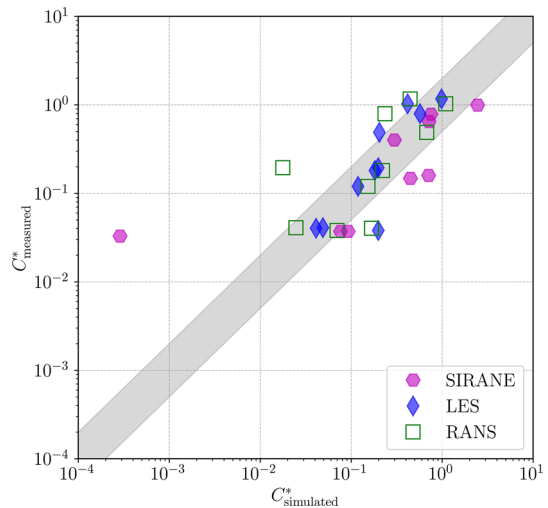


**Fig. 13** Sketch showing streets aligned with  $x$ -axis depicted as blue dashed lines and streets aligned with  $y$ -axis depicted as red dash-dot lines. The streets encompassed within a 180 m radius of a major intersection are only shown. The streets that are aligned with the  $x$ -axis are labelled from 1 to 20 and those that are aligned along the  $y$ -axis are labelled from 21 to 35

**Fig. 14** Comparison of normalized concentration corresponding to source release at  $S_2$ . The shaded region corresponds to a two-factor prediction



aspect ratios in DAPPLE vary, especially due to non-homogeneous building heights and a single representation of  $u_d$  may not be valid for every street.

Using the data obtained from the current RANS simulations, the variation of velocity components in 35 streets as indicated in Fig. 13 are analysed to probe the underlying

assumption in the street network model. For each of these 35 streets, the volume average of velocity components that are aligned with  $x$  and  $y$ -axis of streets are calculated for all 100 RANS simulations. The mean height of the buildings on either side of each canyon is considered to obtain the volume average of velocity. Given highly complex flow structures, the volume of flow within each street is influenced by neighboring streets as well as flow above the canyon, and therefore data shown for each street in a way represents collective behavior.

Statistics of flow velocity for each street in the building region can be calculated from the three-dimensional RANS data as:

$$\langle \phi \rangle_s = \frac{1}{V_s} \iiint_{V_s} \phi_s dV_s \quad \text{where } \phi = u, v, w; \quad (17)$$

$$\sigma_{\phi_s} = \sqrt{\frac{1}{N} \left( \langle \phi \rangle_s - \bar{\phi}_s \right)^2} \quad \text{where } \bar{\phi}_s = \frac{1}{N} \sum_{n=1}^N \langle \phi \rangle_s^n. \quad (18)$$

Here  $\langle \cdot \rangle_s$  denotes the volume average in every street  $s$ ,  $\sigma_{\phi_s}$  is the standard deviation of volume average quantities of velocity components from its ensemble mean  $\bar{\phi}_s$ . Subscript  $s = 1 - 35$  is the street number and superscript  $n = 1 - 100$  denotes a sample instance corresponding to one inlet wind condition. In those expressions,  $V_s$  is the volume of street canyon  $s$ ,  $N = 100$  is the number of LHS samples considered in this study. As the aspect ratio of each street canyon (ratio of length to height of canyon or width to height of canyon) is different, the resulting flow field is inherently different. The variability of flow within each street is useful to understand how much this inherent variation differs from the variation due to changing input parameters. For this, a quantity equivalent to standard deviation is defined as  $\zeta_s$  and its ensemble mean  $\bar{\zeta}_s$  over 100 samples is given by Eq. (19).

$$\bar{\zeta}_s = \frac{1}{N} \sum_{n=1}^N \zeta_s^n \quad \text{where } \zeta_s = \sqrt{\langle \mathbf{u}_s^2 \rangle - \langle \mathbf{u}_s \rangle^2}. \quad (19)$$

Here the mean and standard deviation are computed for the velocity magnitude  $\mathbf{u}$  in every street.

Figure 15 shows the ensemble mean of the volume average of velocity components and their corresponding standard deviation ( $\sigma_s$ ) within each street from 100 samples. It can be seen in Fig. 15a that the street-aligned mean velocity component for  $y$ -streets is higher than that of  $x$ -streets. All the streets show a large standard deviation of the street-aligned velocity component. The variation magnitude is in the same order or even higher than the ensemble mean. This highlights the significant impact of uncertain wind conditions on the street-aligned velocity component. In contrast, the ensemble mean of the vertical velocity component in all the streets is much lower compared to the street-aligned component. Most of the streets show that the mean vertical velocity component is less than 5% of the free stream velocity. It is worth noting that the vertical velocity component varies across the streets. This observation challenges the assumption of uniform vertical exchange velocity commonly used in street network models as mentioned earlier in Eq. (16). Similar to the

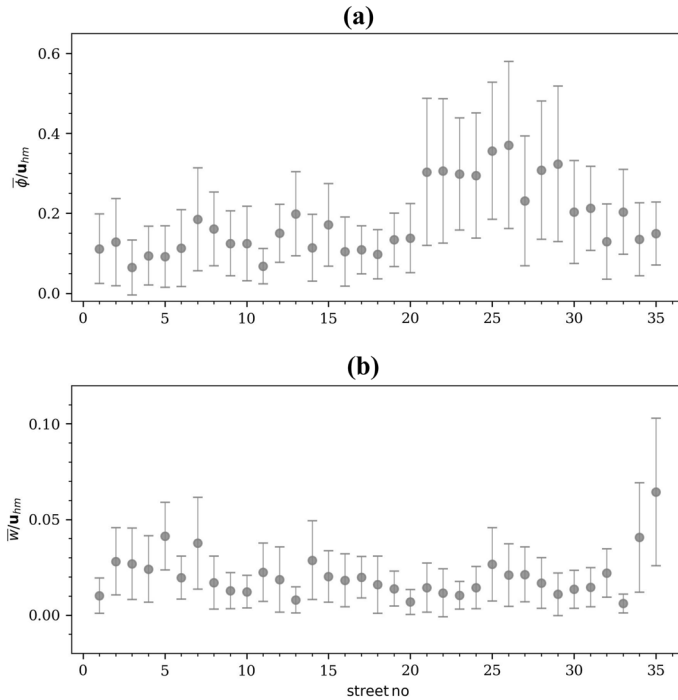


**Fig. 15** Ensemble mean of normalized mean and standard deviation is shown for **a**  $\phi = u$  from 1 to 20 streets that are aligned with the x-axis and  $\phi = v$  from 21 to 35 streets that are aligned with the y-axis, and **b** vertical velocity component from all the streets

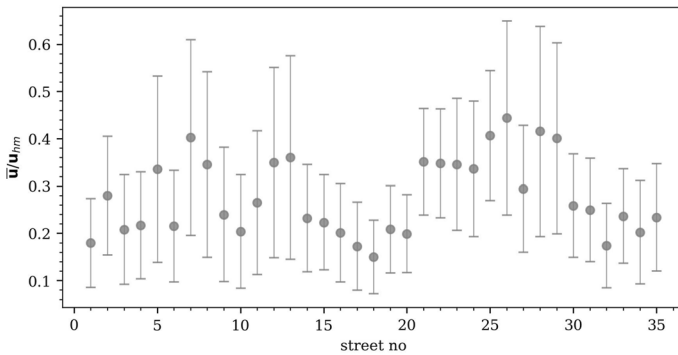


**Fig. 16** Ensemble mean of normalized street volume averaged  $\bar{u}$  and its standard deviation  $\zeta$  is shown for all 35 streets

street-aligned velocity, the standard deviation of the vertical velocity component from 100 samples shows high variability for all the streets.

Figure 16 demonstrates that the standard deviation of volume average velocity in each street,  $\zeta$ , is high and mostly exceeds its average magnitude. This clearly shows the

strong dependency of street-level velocity on inlet conditions. Furthermore, it directly indicates highly non-uniform velocity in street canopies which is assumed to be constant in street network models.

From this brief analysis, we infer that (i) the assumption of constant mean velocity within a canyon does not hold for most of the streets as we observe a large deviation of flow from its mean within each street and (ii) the bulk exchange velocity for the entire building region of interest is not necessarily representative of the transport and mixing processes that occur inside each street. As such it is believed that street network models are not able to fully capture the complex flow nature of heterogeneous canopies which are likely found in many urban environments. It is highly possible that the above limitations contributed to the over-prediction of scalar dispersion in DAPPLE configuration with SIRANE as shown in Fig. 14.

## 5 Conclusions

The input uncertainties are quantified for a passive scalar dispersion in central London using RANS. For this, validation is initially performed for a fixed inlet boundary condition by comparing flow and scalar fields with wind-tunnel experiments and high-fidelity simulation LES. It is found that the flow is under-predicted by RANS while over-predicted by LES when compared to wind-tunnel data. However, the differences are found to be small and the performance of LES and RANS are of similar order. The RANS prediction of scalar at various receiver locations is found to be within the standard deviation bounds of wind-tunnel measurements and also comparable to LES. Along Marylebone Road, the qualitative trend of the scalar is similar for all three types of data. RANS has over-predicted the first peak, and the second peak was shifted to the right, but closer to wind-tunnel data, unlike LES. Overall, RANS prediction of flow and scalar fields with wind-tunnel and LES is satisfactory.

Having established validation in a controlled environment, field measurements are then used as inputs to account for uncertainties at the inlet in RANS. Using Dakota, an uncertainty quantification tool, the inlet uncertainties are propagated in a forward direction to predict the sensitivity of scalar dispersion. A quantity of 100 Latin hypercube samples is used to represent the pdf distribution of wind measurements. RANS simulations are performed to obtain 100 sample mean and 95% CI of the scalar field. For a 3-min average concentration at a specific receiver location, performance measures showed that LES-BTwind is better than RANS and LES-meanwind. Availability of such 3-min time average information at more than one receiver location may help in understanding the sensitivity of location to such performance behavior. For 30-min average concentration at various receiver locations, performance measures indicated that RANS is better than LES-BTwind and LES-meanwind. For relatively longer time-average duration, it shows that inlet uncertainties cannot be ignored for predicting mean scalar in the field. Perhaps, RANS simulations with inlet uncertainties can become a precursor for high-fidelity LES to obtain detailed higher-order statistics for critical parameter inputs. This may then question the usage of

low-order models such as street network models which are generally superior in predicting flow and scalar dispersion with fewer computational resources and time.

Therefore, the mean scalar from wind-tunnel, RANS, LES, and SIRANE are compared at various receiver locations. Unlike SIRANE, RANS and LES are found to be within two-factor bounds of wind-tunnel at several receiver locations. This can be attributed to the assumptions and approximations made in SIRANE that are usually valid for simple regular streets with uniform aspect ratios. To illustrate the complexity of the flow field, data from 100 RANS simulations are used to calculate the volume average of velocity components for 35 streets. In addition, the inherent variation of the flow field from its 100 sample mean within each street is also computed. The ensemble mean showed high variability of volume averaged flow field in each street. This shows that uniform velocity assumption within a street and a single quantity for bulk mass exchange velocity for all the streets may not always adequately represent the complexity of a flow field.

By comparing with high-fidelity LES data, wind-tunnel measurements, field measurements, and the SIRANE model, this study shows the importance of considering inlet uncertainties for predicting mean scalar field using RANS. Despite its inherent limitations in predicting exact turbulence, RANS performance is found to be promising and can be useful in identifying critical parameter range as inputs for high-fidelity simulations or measurements.

## Appendix A Coordinates of source and receiver locations

**Table 3** The coordinates of the source and receiver locations shown in Fig. 2

$S_m$ or $R_n$	$x$	$y$	$z$
$S_2$	-71.2	-140.4	2
$S_5$	-71.2	-212.0	2
$S_6$	-225	-148.0	2
$R_1$	130.7	-148	1.5
$R_2$	117.3	-77.8	1.5
$R_3$	25.9	-79.8	1.5
$R_4^\dagger$	-8.6	-53.8	1.5
$R_5$	-14.4	-48	16.5
$R_6$	76.9	-22.1	1.5
$R_7$	166.3	-14.4	1.5
$R_8^\dagger$	358.6	-16.3	1.5
$R_9$	8.6	55.7	1.5
$R_{10}^\dagger$	-57.7	-73	1.5
$R_{11}$	-100	-70	2
$R_{12}$	40	20	2
$R_{13}$	100	-20	2

For field measurements at  $R_n^\dagger$ ,  $z$  is 2 m

**Acknowledgements** The authors would like to thank Dr. Zheng-Tong Xie of University of Southampton, U.K. and Prof. Alan G Robins of University of Surrey, U.K. for sharing DAPPLE geometry information.

**Author contributions** BB: Conceptualization, Simulation, Data analysis, Methodology, Writing—draft, review & editing. VTN: Conceptualization, Methodology, Data analysis discussions, Writing—review & editing. DW: Geometry creation, Data analysis discussions, Writing—review. JL: Dakota testing, Data analysis discussion, Writing—review & editing.

**Funding** Not applicable

**Data availability** The data will be provided upon request.

**Code availability** The code used is opensource software.

## Declarations

**Conflict of interest** The authors have no conflict of interest.

**Ethics approval** Not applicable.

**Consent to participate** Not applicable.

**Consent for publication** Not applicable.

## References

1. Adams B, Ebeida MM.S.and Eldred, Jakeman J, et al (2014) Dakota, a multilevel parallel object-oriented framework for design optimization, parameter estimation, uncertainty quantification, and sensitivity analysis version 6.7 Theory Manual. Sandia Technical Report SAND2014-4633, July <https://dakota.sandia.gov/sites/default/files/docs/6.7/><https://www.overleaf.com/project/6390585fa8af79090b800e62Theory-6.7.0.pdf>
2. Arnold S, ApSimon H, Barlow J et al (2004) Introduction to the DAPPLE air pollution project. *Sci Total Environ* 332:139–153. <https://doi.org/10.1016/j.scitotenv.2004.04.020>
3. Balogun AA, Tomlin AS, Wood CR et al (2010) In-street wind direction variability in the vicinity of a busy intersection in central London. *Bound-Layer Meteorol* 136:489–513. <https://doi.org/10.1007/s10546-010-9515-y>
4. Barlow J, Dobre A, Smalley RJ et al (2009) Referencing of street-level flows measured during the DAPPLE 2004 campaign. *Atmos Environ* 43(34):5536–5544. <https://doi.org/10.1016/j.atmosenv.2009.05.021>
5. Blocken B, Vervoort R, van Hooff T (2016) Reduction of outdoor particulate matter concentrations by local removal in semi-enclosed parking garages: a preliminary case study for Eindhoven city center. *J Wind Eng Ind Aerodyn* 159:80–98. <https://doi.org/10.1016/j.jweia.2016.10.008>
6. Bohnenstengel SI, Belcher SE, Aiken A et al (2015) Meteorology, air quality, and health in London: the ClearLo project. *Bull Am Meteorol Soc* 96:779–804. <https://doi.org/10.1175/BAMS-D-12-00245.1>
7. Carpentieri M, Robins AG, Baldi S (2009) Three-dimensional mapping of air flow at an urban canyon intersection. *Bound-Layer Meteorol* 133:277–296. <https://doi.org/10.1007/s10546-009-9425-z>
8. Carpentieri M, Salizzoni P, Robins A et al (2012) Evaluation of a neighbourhood scale, street network dispersion model through comparison with wind tunnel data. *Environ Model Softw* 37:110–124. <https://doi.org/10.1016/j.envsoft.2012.03.009>
9. Cimorelli A, Perry S, Venkatram A et al (2004) AERMOD: Description of model formulation. Technical Report, United States Environmental Protection Agency
10. Coceal O, Goulart E, Branford S et al (2014) Flow structure and near-field dispersion in arrays of building-like obstacles. *J Wind Eng Ind Aerodyn* 125:52–68. <https://doi.org/10.1016/j.jweia.2013.11.013>
11. Fellini S, Salizzoni P, Ridolfi L (2021) Vulnerability of cities to toxic airborne releases is written in their topology. *Sci Rep*. <https://doi.org/10.1038/s41598-021-02403-y>

12. García-Sánchez C, Gorlé C (2018) Uncertainty quantification for microscale CFD simulations based on input from mesoscale codes. *J Wind Eng Ind Aerodyn* 176:87–97. <https://doi.org/10.1016/j.jweia.2018.03.011>
13. García-Sánchez C, Van Tendeloo G, Gorlé C (2017) Quantifying inflow uncertainties in RANS simulations of urban pollutant dispersion. *Atmos Environ* 161:263–273. <https://doi.org/10.1016/j.atmosenv.2017.04.019>
14. Grylls T, Le Corne CMA, Salizzoni P et al (2019) Evaluation of an operational air quality model using large-eddy simulation. *Atmos Environ X* 3(100):041. <https://doi.org/10.1016/j.aaea.2019.100041>
15. Hanna S, Chang J (2012) Acceptance criteria for urban dispersion model evaluation. *Meteorol Atmos Phys* 116:133–146. <https://doi.org/10.1007/s00703-011-0177-1>
16. Hargreaves DM, Wright NG (2007) On the use of the  $k - \epsilon$  model in commercial CFD software to model the neutral atmospheric boundary layer. *J Wind Eng Ind Aerodyn* 95:355–369. <https://doi.org/10.1016/j.jweia.2006.08.002>
17. Hertwig D, Soulhac L, Fuka V et al (2018) Evaluation of fast atmospheric dispersion models in a regular street network. *Environ Fluid Mech* 18:1007–1044. <https://doi.org/10.1007/s10652-018-9587-7>
18. Huang ZR, Zhang YJ, Wen YB et al (2022) Synoptic wind driven ventilation and far field radionuclides dispersion across urban block regions: effects of street aspect ratios and building array skylines. *Sustain Cities Soc* 78(103):606. <https://doi.org/10.1016/j.scs.2021.103606>
19. Jurado X, Reiminger N, Vazquez J et al (2021) On the minimal wind directions required to assess mean annual air pollution concentration based on CFD results. *Sustain Cities Soc* 71(102):920. <https://doi.org/10.1016/j.scs.2021.102920>
20. Keshavarzian E, Jin R, Dong K et al (2021) Effect of building cross-section shape on air pollutant dispersion around buildings. *Build Environ* 197(107):861. <https://doi.org/10.1016/j.buildenv.2021.107861>
21. Lim H, Hertwig D, Grylls T et al (2022) Pollutant dispersion by tall buildings: laboratory experiments and Large-Eddy Simulation. *Exp Fluids*. <https://doi.org/10.1007/s00348-022-03439-0>
22. Liu Z, Barlow JF, Chan PW et al (2019) A review of progress and applications of pulsed Doppler wind LiDARs. *Remote Sens* 11:2522. <https://doi.org/10.3390/rs11212522>
23. Lucas DD, Gowardhan A, Cameron-Smith P et al (2016) Impact of meteorological inflow uncertainty on tracer transport and source estimation in urban atmospheres. *Atmos Environ* 143:120–132. <https://doi.org/10.1016/j.atmosenv.2016.08.019>
24. Margheri L, Sagaut P (2016) A hybrid anchored-ANOVA-POD/Kriging method for uncertainty quantification in unsteady high-fidelity CFD simulations. *J Comput Phys* 324:137–173. <https://doi.org/10.1016/j.jcp.2016.07.036>
25. OpenFOAM (2020) <https://www.openfoam.com/news/main-news/openfoam-v20-12>. Accessed Jan 2021
26. Pardyjak E, Brown M (2003) QUIC-URB v.1.1: theory and users guide. Report LA-UR-07-3181. Los Alamos National Laboratory, Los Alamos, NM, USA
27. Ricci A, Kalkman I, Blocken B et al (2020) Impact of turbulence models and roughness height in 3D steady RANS simulations of wind flow in an urban environment. *Build Environ* 171(106):617. <https://doi.org/10.1016/j.buildenv.2019.106617>
28. Scire J, Strimaitis D, Yamartino R (2000) A user's guide for CALPUFF dispersion model (Version 5). Technical Report, Earth Tech Inc URL [http://www.src.com/calpuff/download/CALPUFF\\_Users\\_Guide.pdf](http://www.src.com/calpuff/download/CALPUFF_Users_Guide.pdf)
29. Shim G, Prasad D, Elkins C et al (2019) 3D MRI measurements of the effects of wind direction on flow characteristics and contaminant dispersion in a model urban canopy. *Environ Fluid Mech* 19:851–878. <https://doi.org/10.1007/s10652-019-09676-y>
30. Soulhac L, Salizzoni P, Cierco FX et al (2011) The model SIRANE for atmospheric urban pollutant dispersion; part I, presentation of the model. *Atmos Environ* 45(39):7379–7395. <https://doi.org/10.1016/j.atmosenv.2011.07.008>
31. Soulhac L, Salizzoni P, Mejean P et al (2012) The model SIRANE for atmospheric urban pollutant dispersion; PART II, validation of the model on a real case study. *Atmos Environ* 49:320–337. <https://doi.org/10.1016/j.atmosenv.2011.11.031>
32. Soulhac L, Salizzoni P, Mejean P et al (2013) Parametric laws to model urban pollutant dispersion with a street network approach. *Atmos Environ* 67:229–241. <https://doi.org/10.1016/j.atmosenv.2012.10.053>
33. Soulhac L, Lamaison G, Cierco FX et al (2016) SIRANERISK: modelling dispersion of steady and unsteady pollutant releases in the urban canopy. *Atmos Environ* 140:242–260. <https://doi.org/10.1016/j.atmosenv.2016.04.027>

34. Soulhac L, Nguyen C, Volta P et al (2017) The model SIRANE for atmospheric urban pollutant dispersion. PART III: validation against NO<sub>2</sub> yearly concentration measurements in a large urban agglomeration. *Atmos Environ* 167:377–388. <https://doi.org/10.1016/j.atmosenv.2017.08.034>
35. Tominaga Y, Iizuka S, Imano M et al (2013) Cross comparisons of CFD results of wind and dispersion fields for MUST experiment: evaluation exercises by AIJ. *J Asian Archit Build Eng.* <https://doi.org/10.3130/jaabe.12.117>
36. United Nations (n.d.) Take action for the sustainable development goals - United Nations Sustainable Development. <https://www.un.org/sustainabledevelopment/sustainable-development-goals/>. Accessed 4 Aug 2022
37. Volpiani PS, Meyer M, Franceschini L et al (2021) Machine learning-augmented turbulence modeling for RANS simulations of massively separated flows. *Phys Rev Fluids* 6(064):607. <https://doi.org/10.1103/PhysRevFluids.6.064607>
38. Wang A, Fallah-Shorshani M, Xu J et al (2016) Characterizing near-road air pollution using local-scale emission and dispersion models and validation against in-situ measurements. *Atmos Environ* 142:452–464. <https://doi.org/10.1016/j.atmosenv.2016.08.020>
39. Wieringa J (1992) Updating the Davenport roughness classification. *J Wind Eng Ind Aerodyn* 41:44–357–368. [https://doi.org/10.1016/0167-6105\(92\)90434-C](https://doi.org/10.1016/0167-6105(92)90434-C)
40. Wise DJ, Boppana VBL, Li KW et al (2018) Effects of minor changes in the mean inlet wind direction on urban flow simulations. *Sustain Cities Soc* 37:492–500. <https://doi.org/10.1016/j.scs.2017.11.041>
41. Wood C, Arnold SJ, Balogun AA et al (2009) Dispersion experiments in Central London: the 2007 DAPPLE project. *Bull Am Meteor Soc* 90:955–970. <https://doi.org/10.1175/2009BAMS2638.1>
42. Xie ZT (2011) Modelling street-scale flow and dispersion in realistic winds-towards coupling with mesoscale meteorological models. *Bound-Layer Meteorol* 141:53–75. <https://doi.org/10.1007/s10546-011-9629-x>
43. Xie ZT, Castro I (2006) LES and RANS for turbulent flow over arrays of wall mounted cubes. *Flow Turbul Combust* 76:291–312. <https://doi.org/10.1007/s10494-006-9018-6>
44. Xie ZT, Castro IP (2009) Large-eddy simulation for flow and dispersion in urban streets. *Atmos Environ* 43:2174–2185. <https://doi.org/10.1016/j.atmosenv.2009.01.016>

**Publisher's Note** Springer Nature remains neutral with regard to jurisdictional claims in published maps and institutional affiliations.

Springer Nature or its licensor (e.g. a society or other partner) holds exclusive rights to this article under a publishing agreement with the author(s) or other rightsholder(s); author self-archiving of the accepted manuscript version of this article is solely governed by the terms of such publishing agreement and applicable law.

## Authors and Affiliations

**Bharathi Boppana<sup>1</sup> · Vinh-Tan Nguyen<sup>1</sup> · Daniel J. Wise<sup>1</sup> · Jason Yu Chuan Leong<sup>1</sup>**

Vinh-Tan Nguyen  
nguyenvt@ihpc.a-star.edu.sg

Daniel J. Wise  
daniel-wise@ihpc.a-star.edu.sg

Jason Yu Chuan Leong  
jason-leong@ihpc.a-star.edu.sg

<sup>1</sup> Institute of High Performance Computing (IHPC), Agency for Science, Technology and Research (A\*STAR), 1 Fusionopolis Way, #16-16 Connexis, 138632 Singapore, Republic of Singapore